JOURNAL OF MECHANICAL ENGINEERING, SCIENCE, AND INNOVATION
ITATS
Research Article

Corrosion-Induced Failure Mechanisms in Bio-Nano Hybrid Coatings for Structural Applications

Journal of Mechanical Engineering, Science, and Innovation
e-ISSN: 2776-3536
2026, Vol. 6, No. 1
DOI: 10.31284/j.jmesi.2026.v6i1.8625
ejurnal.itats.ac.id/jmesi

Maulidia Hendriani[1], Andoko Andoko[1*], Riduwan Prasetya[1], and Yahya Zakaria[1]

[1]Department of Mechanical and Industrial Engineering, Faculty of Engineering, State University of Malang, Jl Semarang 5, Malang City, Indonesia

Corresponding author:
Andoko andoko
State University of Malang, Indonesia
Email: andoko.ft@um.ac.id

Abstract

This study examines the corrosion resistance performance and failure mechanisms of a hybrid coating system based on castor oil and nano-SiO_2 with three particle size variations (20 nm, 100 nm, and 500 nm) applied to ASTM A36 steel. We compared uncoated samples with three coating variants to evaluate the effect of nano-SiO_2 size on corrosion resistance and damage development. Coating resistance was tested using potentiodynamic polarization, FTIR analysis, corrosion morphology characterization, and coating thickness measurements. Compared to uncoated steel, the formulation with 100 nm nano-SiO_2 provided the greatest improvement, with a three-order decrease in corrosion current density (i_{corr} = 1.33×10^{-8} A/cm^2) and a shift in corrosion potential toward a more positive direction, accompanied by stable surface morphology and minimal chemical changes. This effectiveness is achieved through homogeneous particle dispersion, which produces a dense barrier structure and tortuous diffusion pathways without a significant increase in thickness. Failure mechanism analysis shows that small particle sizes (20 nm) trigger porous barrier breakdown due to nano-silica aggregation, while large particles (500 nm) cause coating cracking and localized pitting due to sedimentation and excessive thickness. In contrast, the 100 nm size stabilizes the passive film and suppresses pit initiation. These findings confirm that controlling the size and dispersion of nano-SiO_2 not only improves corrosion resistance but also determines the dominant failure pathway in coatings. This research contributes to the development of sustainable bio-nano coatings for structural applications by highlighting the importance of microstructural reinforcement and understanding failure mechanisms in designing high-resistance coating systems.

Keywords: *: Hybrid Coating, Castor Oil, Nano-SiO_2, Failure Mechanism*

Received: January 14, 2026; Received in revised: February 27, 2026; Accepted: March 12, 2026
Handling Editor: Iftika Wardani and Michele Bici

INTRODUCTION

Corrosion is one of the main causes of structural damage to metal materials in various industrial sectors around the world [1]. This degradation process occurs through

electrochemical reactions between metals and the environment, resulting in a gradual decrease in the mechanical strength of materials [2]. Global economic losses due to corrosion are reported to reach trillions of dollars annually and have a significant impact on industrial operational efficiency. The oil and gas, transportation, marine, and power generation sectors are among the industries with the highest corrosion risk [3]. The impact of corrosion not only causes financial losses, but also threatens work safety and increases the possibility of fatal accidents [4]. Failure analysis shows that most structural damage to heavy industrial facilities originates from undetected corrosion damage [5], [6], [7]. Corrosion on metal components that experience repeated loading accelerates the initiation of cracks and the propagation of material damage [8]. This problem poses a major challenge for the field of materials engineering, particularly in the development of protective coating systems capable of functioning in aggressive environments. Coating technologies with long-term resistance to corrosion and mechanical degradation are needed. Research on multifunctional coatings continues to be developed to address this issue.

Various approaches have been developed to improve the corrosion resistance of metals, particularly through the modification of polymer-based coatings and nanoparticles. Alam et al. [9] reported that a combination of SiO_2 and ZnO nanoparticles in an epoxy matrix can increase the hardness and corrosion resistance of coatings. González-Reyna et al. [10] showed that the size of nano-silica particles significantly affects corrosion protection performance, with smaller sizes providing more homogeneous particle distribution. Wang et al. [11] found that amino-silica modification in epoxy resin increases electrical impedance and ionic resistance to corrosive media. Meanwhile, Xu et al. [12] successfully improved coating performance by adding hydrophobic nano-silica to the epoxy system. Recent research also shows that the addition of nano-SiO_2 to the epoxy matrix can achieve impedance of up to 10^{12}–10^{21} $\Omega \cdot cm^2$ at an optimal composition of around 2.5 wt%, although particle size variations have not been explored in depth [13]. On the other hand, another study developed a non-isocyanate polyurethane (NIPU) coating based on castor oil with the addition of Fe_3O_4@SiO_2–NH_2 nanocomposites, which provided biodegradability, antifouling, and initial corrosion resistance properties, but the impedance value was still relatively low [14]. Nevertheless, the majority of previous studies still focus on synthetic polymer-based coating systems and have not integrated renewable resources such as vegetable oil. There have been few studies combining castor oil as a coating base material with nano-SiO_2 in the context of testing material fatigue due to dynamic loads. In addition, there is almost no literature that examines the effect of nano-SiO_2 surface size on coating performance in cyclic and corrosive environments. Thus, there is an important research gap in the development of hybrid coating systems that combine material sustainability and mechanical resistance. This study aims to address this gap through a new approach that combines vegetable oil and nano-silica as coating materials.

Hybrid coating systems that utilize vegetable oil and nano-silica are a potential solution to the challenges of corrosion and structural fatigue. Jatropha oil, as one type of abundant local vegetable oil, has a high hydroxyl content that enables cross-linking in coating systems [15]. The use of castor oil as a coating base material provides an environmentally friendly and renewable alternative to petrochemical-based polymers [16]. Meanwhile, nano-SiO_2 acts as an inorganic filler that increases resistance to corrosive ion penetration and strengthens the mechanical structure of the coating. The combination of the two is expected to produce a coating system that is not only resistant to corrosion but also to repeated cyclic loading. Castor oil and nano-silica-based formulations offer the potential to reduce production costs, improve sustainability, and extend the service life of metal components. In addition, variations in the mesh size of nano-SiO_2 provide opportunities to control the microstructure and diffusion

characteristics of the coating with greater precision. The advantages of this hybrid system also lie in its design flexibility and compatibility with structural steels such as ASTM A36. Given the issues outlined above, this approach is believed to have a significant impact on the development of future coating technologies. Therefore, this study positions hybrid coating as a promising approach for long-term corrosion protection.

This study used ASTM A36 steel as a test substrate to mimic the conditions of structural components in the manufacturing and construction industries. The coating material was composed of a mixture of castor oil as the main component, combined with SiO_2 nanoparticles. The main variable that was varied was the surface size of the nano-SiO_2, namely 20 nm, 100 nm, and 500 nm, to evaluate its effect on coating performance. The coating process was carried out through mechanical mixing and manual application on the prepared steel surface. All samples were conditioned in a room temperature environment to ensure natural drying reactions without external thermal activation. Characterization of the coating properties was carried out through corrosion resistance testing using the Electrochemical Impedance Spectroscopy (EIS) method and potentiodynamic polarization test. Surface morphology analysis was performed using macroscopic corrosion morphology. All data obtained were statistically analyzed to determine the significant effects of the variables studied. The methods used were designed to ensure the validity of the data in evaluating corrosion resistance and coating strength.

This research is expected to provide new insights into the development of renewable-based coating systems that are highly resistant to corrosion and dynamic loads. The developed coating formulation is projected to increase the service life of structural metals in industrial applications that come into contact with aggressive environments. The addition of nano-SiO_2 in the right particle size is believed to strengthen the protective coating structure and inhibit the diffusion of corrosive media. In addition to contributing to coating technology, the results of this study also have the potential to encourage the use of local natural materials such as castor oil as an alternative source of resin. The long-term implications of this research include cost efficiency in metal structure maintenance and improved operational safety in the heavy industry sector. In the context of education, this research can be a learning resource for engineering students in understanding the integration between materials science and corrosion protection engineering. On the other hand, the development of comprehensive characterization methods also contributes to strengthening laboratory literacy in academic environments. The knowledge generated from this study can be used as a basis for further research in the field of multifunctional coatings. The results of this study can also support the formulation of green industrialization policies based on renewable resources. This research not only provides theoretical contributions but also has practical applications in industry and higher education.

METHODS AND ANALYSIS

Materials

Low carbon steel used as a substrate was ASTM A36. Steel sheets were cut into rectangular specimens measuring 10 mm × 10 mm × 2 mm for immersion and coating evaluation. The base coat was prepared using castor oil (CV IndoCastor, Indonesia) due to its rich hydroxyl composition, which facilitates polar interaction with the steel surface. Nano-silica (SiO_2) powder (Sigma-Aldrich, 99.5% purity, average particle size 20 nm, 100 nm, and 500 nm) was used as an inorganic filler to enhance the barrier effect of the oil coating. The top coat used bisphenol-A epoxy resin (Epikote 828) and a polyamide-based hardener (Epikure 3402), mixed at a resin-to-hardener ratio of 2:1 by weight. Acetone, ethanol, and sodium chloride (NaCl) were used for cleaning and preparing the corrosion solution.

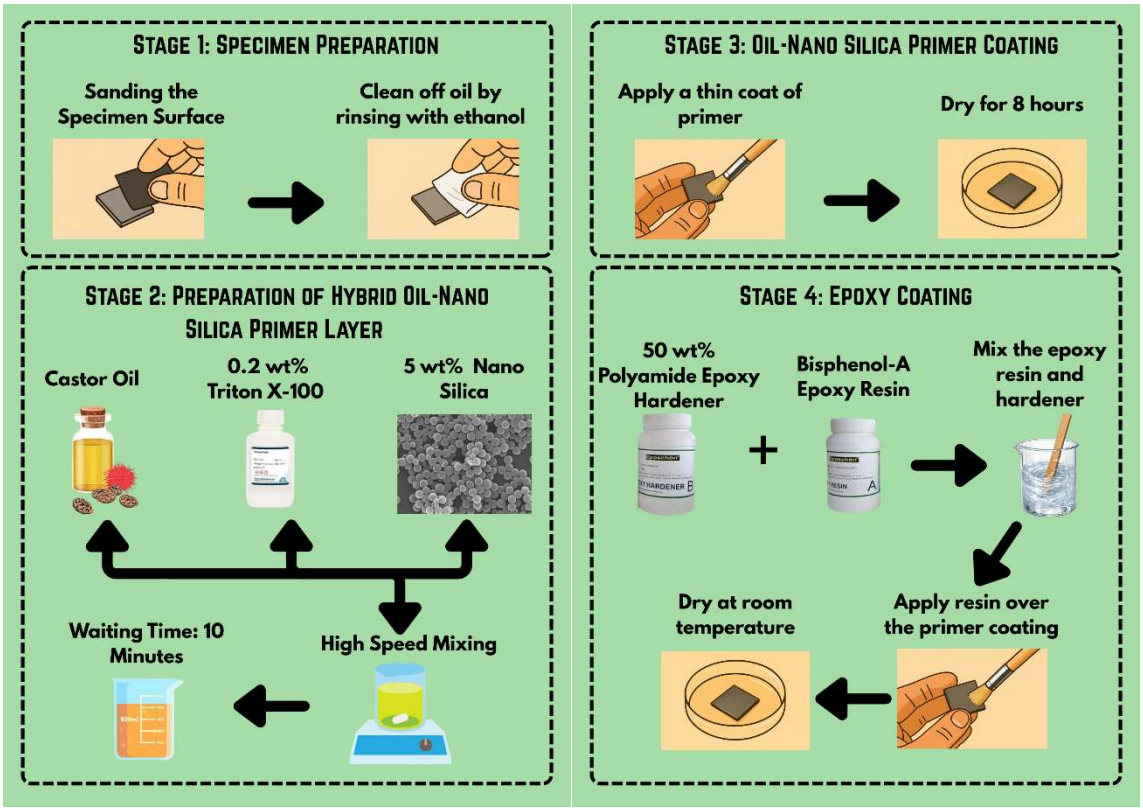

Figure 1. Schematic Diagram of the Primer Preparation and Specimen Coating Process

Steel Surface Preparation

The overall experimental workflow, including primer preparation and specimen coating procedures, is schematically illustrated in Figure 1. Before the coating process, all steel specimens were manually polished using silicon carbide abrasive paper (grit 400–600) to remove surface oxides and contaminants. The samples were then cleaned of oil by rinsing with ethanol 70%, and in this study a total volume of 100 mL was used to ensure sufficient coverage and effective degreasing of all specimen surfaces. The dried specimens were stored in a desiccator for 2 days prior to the coating process to prevent moisture absorption and surface contamination.

Preparation of the Oil-Nano Silica Hybrid Primer

Nano-silica is dispersed into castor oil at a concentration of 5% by weight relative to the oil mass. In this study, a total volume of 50 mL of castor oil was used as the dispersion medium. The mixture was stirred using a magnetic stirrer at a speed of 500 rpm for 30 minutes at room temperature to achieve uniform dispersion. To prevent nanoparticle aggregation, 0.2% by weight of Triton X-100 was added as a non-ionic surfactant. The oil-nano mixture was then left for 10 minutes before application.

Hybrid Oil-Nano Silica Primer Coating

The oil-nano silica hybrid mixture was applied to the steel surface using a brush in a single thin layer. The samples were dried in air at room temperature for 8 hours to allow partial absorption and bonding to the metal surface.

Epoxy Coating

After the primer layer dried, epoxy resin and hardener were mixed in a 2:1 weight ratio and applied using the same brush technique. The epoxy resin was applied in a single, even coat with a target dry film thickness of 100–150 µm. The coated samples were dried at room temperature (25–28°C) for 24 hours, followed by further drying in an oven at 60°C for 2 hours to ensure optimal cross-linking.

Table 1. Design of Experiments

Samples	Treatment
S1	Steel
S2	Steel+ SiO2 (20nm)+Castrol Oil+Epoxy
S3	Steel+ SiO2 (100nm)+Castrol Oil+Epoxy
S4	Steel+ SiO2 (500nm)+Castrol Oil+Epoxy

Design of Experiments

The experimental design and sample configurations used in this study for the systematic evaluation of the effect of nano-silica particle size on the corrosion protection performance of coating systems are summarized in Table 1.

Full Immersion Test (Static)

Coated and uncoated specimens were completely immersed in a 3.5% NaCl solution at room temperature for a total of 21 days. In this study, 80 mL of 3.5% NaCl solution was used for each immersion setup to ensure full submersion of the specimens. Samples were placed in glass containers with airtight lids to prevent evaporation. After immersion, samples were rinsed with deionized water, dried, and stored in a desiccator for further analysis.

Surface and Structure Analysis

Potentiodynamic Polarization Test

Potentiodynamic polarization test is used to determine the corrosion behavior of a material by measuring the relationship between electrical potential and current density in an electrolyte medium [17]. In this study, the test was conducted using an Autolab PGSTAT204 Potentiostat (Metrohm Autolab) equipped with NOVA software for electrochemical analysis. The instrument operates with a wide potential range (±10 V), high current resolution up to picoampere level, and precise potential control, enabling accurate detection of electrochemical responses during polarization scanning. The basic principle is to gradually control the potential of the sample and record the resulting current. The test results are displayed in the form of a Tafel curve, which provides information about the corrosion potential (E_{corr}) and the corrosion current density (I_{corr}). The equation commonly used to calculate the corrosion rate is given in Equation (1).

$$CR = \frac{K \cdot I_{corr} \cdot EW}{\rho \cdot A} \quad (1)$$

with CR= corrosion rate, K = constanta, I_{corr} = corrosion current, EW = equivalent weight, ρ = density, and A = surface area [18]. Based on this equation, the higher the value I_{corr}, the faster the corrosion rate. This test can also identify the dominant corrosion mechanism, such as pitting, general corrosion, or passivation [19]. Its advantage is that it can provide quantitative data with high precision. However, this method requires stable electrochemical control. Therefore, potentiodynamic polarization has become one of the standard methods for analyzing the corrosion resistance of materials.

Fourier Transform Infrared Spectroscopy (FTIR)

Fourier Transform Infrared Spectroscopy (FTIR) is a characterization method used to identify chemical functional groups in materials based on their interaction with infrared radiation [20]. In this study, the analysis was conducted using a Thermo Scientific Nicolet iS10 FTIR Spectrometer (Thermo Fisher Scientific, USA) with a spectral range of 4000–400 cm^{-1} and a resolution of 4 cm^{-1}, equipped with a DTGS detector and ATR sampling accessory. The principle of operation is that molecules absorb radiation at specific wavelengths corresponding to atomic bond vibrations. The resulting spectrum data is in the form of a graph of transmittance or absorbance against wavenumber (cm^{-1}).

To relate the spectral position to the physical properties of infrared radiation, the wavenumber $\tilde{\nu}$is mathematically defined as a function of wavelength and frequency. This relationship is expressed in Equation (2).

$$\tilde{\nu}=\frac{1}{\lambda}=\frac{v}{c} \quad (2)$$

where $\tilde{\nu}$ = wave number, λ = wave length, v = frequency, dan c = speed of light. Each peak in the FTIR spectrum indicates a type of bond such as -OH, -C=O, -C-H, and so on. This technique is widely used to analyze coatings, composites, and corrosion degradation. FTIR results can indicate chemical changes on the surface of a material. FTIR can also confirm the presence of corrosion or oxidation compounds on metal materials. This method is very important for supporting the interpretation of a material's chemical properties.

Macroscopy Corrosion Morphology

Macroscopic corrosion morphology is a characterization method that involves visual observation or the use of a high-resolution camera to analyze damage patterns on the surface of materials [21]. This technique allows for the identification of corrosion types such as uniform corrosion, pitting corrosion, intergranular corrosion, or galvanic corrosion. The principle of this method is based on comparing surface conditions before and after corrosion testing to evaluate morphological changes. In the present study, macroscopic images were captured using a high-resolution digital imaging device under controlled and uniform LED illumination to ensure consistent brightness and contrast. The specimens were placed in a horizontal position, and images were acquired from a perpendicular top-view orientation to minimize perspective distortion. The camera was maintained at a fixed focal distance to ensure consistent magnification, and a calibrated measurement scale was included in each image to provide dimensional reference. This controlled imaging configuration enhances reproducibility and improves the reliability of morphological interpretation. Furthermore, this technique facilitates correlation between observed damage morphology and the underlying corrosion mechanisms.

Coating Thickness Measurement

Thickness measurement of coatings using a micrometer gauge is performed to determine the thickness of the protective layer applied to the material [22]. The measurement was conducted using an EXTECH Ultrasonic Thickness Gauge TKG100 equipped with a DK5537 transducer (50 MHz), which operates based on the ultrasonic pulse-echo principle, where high-frequency sound waves are transmitted into the material and the reflected signals are converted into thickness values. Coating thickness is important because it directly affects the corrosion resistance and mechanical properties of the material. The coating thickness is calculated based on these measurements by taking the difference between the total coated thickness and the original substrate thickness. This relationship is mathematically expressed in Equation (3).

$$t=L_{total}-L_{substrat} \quad (3)$$

where t = coating thickness, L_{total} = material size with coating, dan $L_{substrat}$ = material size without coating. The greater the value of t , the more effective the layer is in inhibiting penetration by the corrosive environment. Measurements are taken at several points to obtain the average thickness. The measurement results can be compared with the ISO 12944 standard to ensure coating quality. This technique has advantages in terms of accuracy, simplicity, and non-destructiveness.

Scanning Electron Microscopy–Energy Dispersive X-ray Spectroscopy (SEM–EDX)

Surface characterization using Scanning Electron Microscopy–Energy Dispersive X-

ray Spectroscopy (SEM–EDX) aims to identify elemental composition, detect corrosion product formation, and analyze element distribution on the coating surface after exposure to aggressive environments [23]. The test was conducted using a Hitachi TM4000Plus operated at an acceleration voltage of 20 kV in Backscattered Electron (BSE) mode with 500× magnification. EDX analysis was performed only on coated specimens, as SiO_2 nanoparticles were exclusively incorporated within the coating layer. Through this analysis, chemical changes such as an increase in oxygen content due to oxidation and the presence of aggressive ions can be detected locally. In addition, EDX is used to show the distribution of SiO_2 particles through silicon (Si) and oxygen (O) element mapping, so that the homogeneity of inorganic filler dispersion in the matrix can be evaluated quantitatively and qualitatively. This SiO_2 distribution information is important for assessing the effectiveness of layer reinforcement, identifying potential particle agglomeration, and correlating it with the location of degradation or failure initiation on the material surface.

RESULTS AND DISCUSSIONS

Corrosion Resistance Based on Electrochemical Response

The results of the potentiodynamic polarization test showed significant variations in the corrosion potential (E_{corr}) and corrosion current density (i_{corr}) values between samples, as summarized in Table 2. The uncoated specimen (S1) had the most negative E_{corr} of −0,535 V and the highest i_{corr} of $2{,}208\times10^{-5}$ A/cm^2, indicating the highest corrosion rate due to direct exposure to chloride ions. This is quantitatively confirmed by the corrosion rate value of 0,257 mm/year for S1, which is the highest among all samples, reflecting severe material degradation in the absence of protective coating. After applying the hybrid coating system, all of the coated samples showed a shift toward more positive E_{corr} values and a substantial decrease in i_{corr}, confirming improved corrosion resistance. The corrosion rate decreased drastically for all coated specimens, with S2 showing 0,0037211 mm/year, S4 showing 0,0040608 mm/year, and S3 exhibiting the lowest value of 0,00015483 mm/year, as presented in Table 2. Sample S3 with a particle size of 100 nm showed the best performance with Ecorr of −0,371 V and the lowest icorr of $1{,}330\times10^{-8}$ A/cm^2. Compared to the uncoated steel (0,257 mm/year), the corrosion rate of S3 is reduced by more than three orders of magnitude, demonstrating the highest protection efficiency among the tested systems. Consistent with these electrochemical parameters, the tafel slope behavior of S3 exhibits a flatter anodic-cathodic curve shift, indicating an increase in charge transfer resistance, as shown in Figure 2. The difference in performance between samples shows that the size of SiO_2 nanoparticles affects the barrier properties of the coating and the distribution of fillers in the matrix.

The increase in corrosion resistance in nano-SiO_2 coated samples is due to the double barrier effect between the organic network and the inorganic phase that is formed. A study by Alam et al. [9] shows that the addition of nano-SiO_2 increases hardness and corrosion resistance due to an increase in cross-link density and a reduction in micro pores in the coating. These results are in line with the report by González-Reyna et al. [10], which confirms that the size of silica nanoparticles affects the homogeneity of dispersion and the effective thickness of the barrier. In addition, the results of research by Hussain et al. [13] show that a uniform distribution of nano-SiO_2 can increase impedance through the mechanism of closing ion diffusion pathways. These findings support the best performance of S3 (100 nm), as the medium particle size allows for even distribution without significant aggregation. The consistently lower corrosion rate values of the coated samples, particularly S3, further verify that the optimized nanoparticle size effectively minimizes electrolyte penetration and slows the metal dissolution kinetics. The correlation between nano SiO_2 size and decreasing i_{corr} indicates that the main protection mechanism is an increase in charge transfer resistance and the blocking of

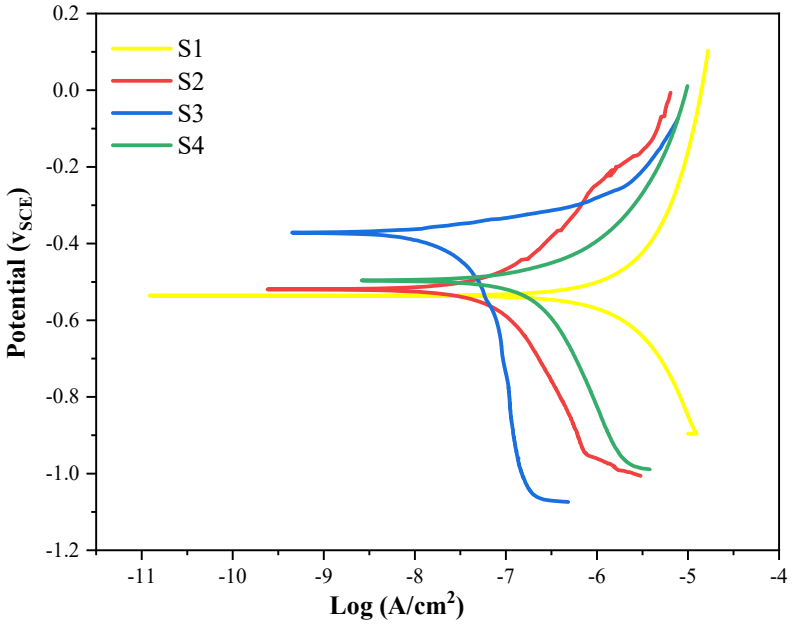

Figure 2. Potentiodynamic Polarization Curve of ASTM A36 Steel Without Coating and Coating with Different SiO_2 Particle Sizes

Table 2. Potentiodynamic Polarization Test Results Data

Samples	E_{corr}	i_{corr}	β_c	β_a	Corrosion Rate
	(v)	(A/cm^2)	(V/dec)	(V/dec)	mm/year
S1	-0.535	2.208×10^{-5}	2.469	6.065	0.257
S2	-0.519	3.202×10^{-7}	5.097	0.473	0.0037211
S3	-0.371	1.330×10^{-8}	0.195	0.042	0.00015483
S4	-0.496	3.489×10^{-7}	0.996	0.183	0.0040608

chloride ion penetration through a denser coating structure [24].

Chemical Identification of Protective Functional Groups

As shown in Figure 3, the FTIR spectrum results reveal the presence of several characteristic peaks from castor oil and its interaction with nano-SiO_2. The strong absorption band around 3400 cm^{-1} indicates the stretching vibration of the –OH group from castor oil triglycerides. The peak at 1735 cm^{-1} is identified as the C=O stretching vibration of the ester group, while the band in the range of 1080–1120 cm^{-1} indicates the presence of the Si–O–Si bond characteristic of the silica structure. The intensity of the Si–O–Si peak increased with the addition of nano-SiO_2, especially in sample S3, which showed the best integration between the organic and inorganic phases. After the corrosion test, a small shift appeared in the –OH and C=O bands, indicating chemical interaction between the corrosion products ($Fe(OH)_2$, FeOOH) and the coating matrix.

The changes in intensity and peak shifts in FTIR indicate the formation of a cross-linked network between the hydroxyl groups of castor oil and the silanol groups on the surface of nano-SiO_2. This mechanism results in a denser composite structure and increases resistance to water diffusion. Sulthana et al. [14] reported that similar interactions in castor oil-based NIPU and nano-SiO_2 systems improve the anticorrosive properties and thermal stability of the coating. Furthermore, the FTIR results can also be attributed to the formation of a passivation layer at the metal interface, as described in a study on corrosive atmospheres by Wang et al. [25], where increased –OH bands after NaCl exposure indicate the formation of protective oxyhydroxides. This phenomenon explains why the coating with optimal SiO_2 dispersion (S3) showed the smallest peak

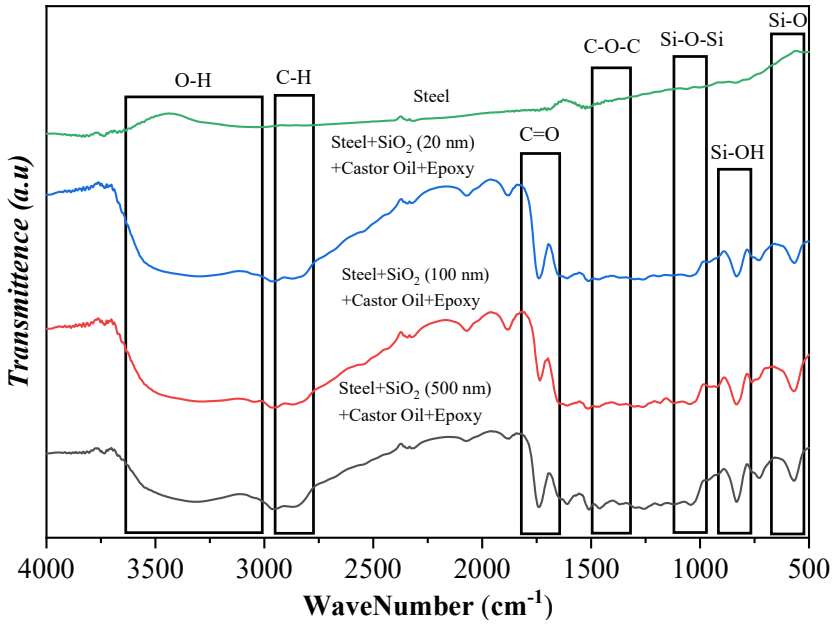

Figure 3. Comparison Curve of Functional Groups from ASTM A36 Steel Without Coating and Coating with DifferentSiO_2Size Variations

shift, indicating the least chemical degradation. Thus, the FTIR results confirm that the chemical bond between castor oil and silica plays an important role in resisting ion penetration and stabilizing the coating structure during the corrosion process.

Post-Corrosion Surface Morphology

As shown in Figure 4, morphological observation of the surface using macroscopy reveals clear differences between uncoated and coated samples. The uncoated steel surface (S1) exhibited uniform corrosion and deep pits after 7 days of immersion in a 3.5% NaCl solution, indicating a general corrosion mechanism and active pitting. In con-

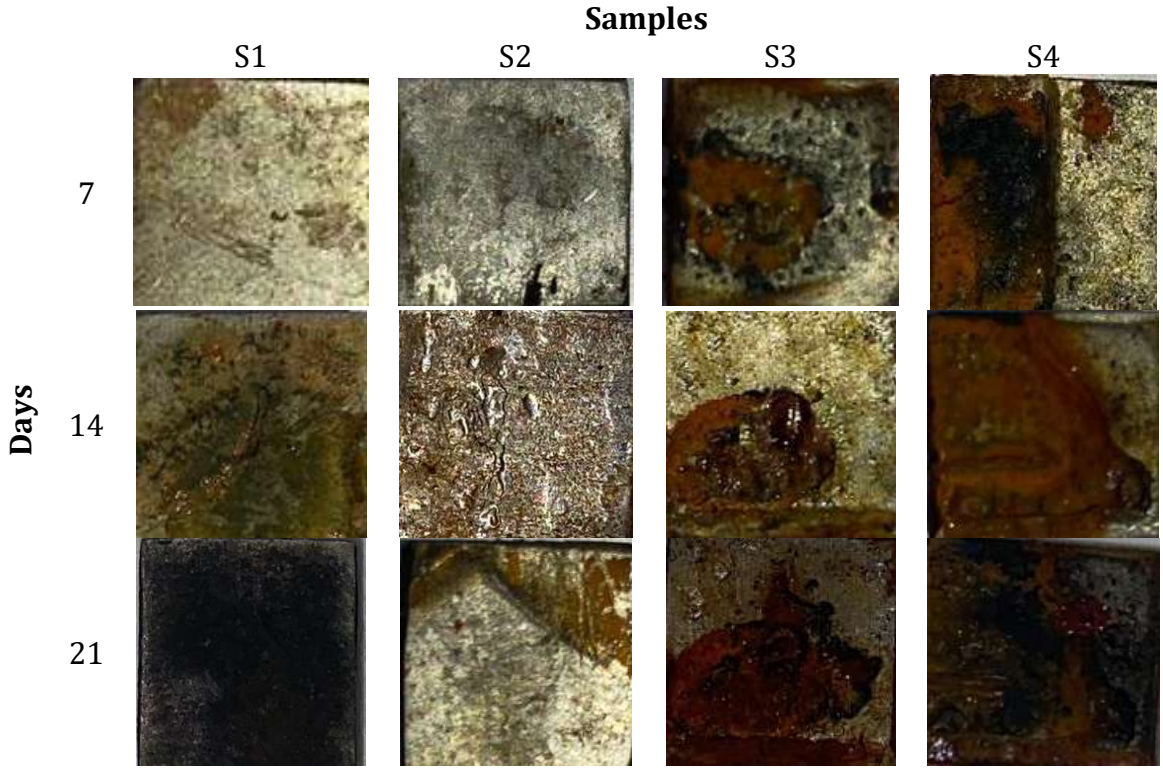

Figure 4. Comparison of Macroscopic Images of Uncoated ASTM A36 Steel and Coated Steel with Different SiO_2 Sizes

Table 3. Coating Thickness

Samples	Thickness (μm)
S1	0
S2	±578
S3	±443
S4	±505

trast, the hybrid-coated samples showed lighter color changes and a reduction in the number of pits. Sample S2 (20 nm) exhibited a rough surface with indications of nanoparticle aggregation, while S3 (100 nm) had a more homogeneous surface and showed only shallow micro pits. S4 (500 nm) displayed a more cracked coating with localized corrosion areas around surface defects. Overall, S3 showed the most stable morphology with little evidence of chloride ion penetration.

These morphological differences are consistent with the corrosive diffusion model in composite coatings. ISO 12944-5 states that microcracks or surface heterogeneity can be the main entry points for aggressive ions, making coating homogeneity and thickness critical parameters [26]. These results are consistent with the research by Hedayatzadeh et al. [24], which shows that pore filling with SiO_2 nanoparticles can reduce pit density by up to 80% compared to coatings without fillers. Furthermore, research by Malla et al. [25] emphasizes that the accumulation of corrosion products in the coating pores can form a secondary barrier that slows down pit propagation. This mechanism explains the surface pattern of S3, which shows a combination of solid layers and shallow pits. Therefore, the more homogeneous morphology of S3 confirms the role of medium-sized nano-SiO_2 dispersion in improving the coating microstructure and slowing down the pitting corrosion mechanism.

Consistency and Effectiveness of Coating Thickness

Measurements of thickness using a micrometer gauge showed variations in thickness between samples. S2 had an average thickness of ±578 μm, S3 was ±443 μm, and S4 was ±505 μm. These differences may be due to the degree of dispersion of nano-SiO_2 during application. The excessive thickness of S2 resulted in an uneven coating, while the optimal thickness of S3 produced a more compact and homogeneous coating. The coating thickness was found to affect the electrochemical performance and surface observation results, with S3 showing a balance between mechanical flexibility and barrier density. The thickness value of S3 is still within the ISO 12944-5 recommendation range for multi-layer coating systems with high resistance to atmospheric corrosion.

According to ISO 12944-5 standards, coating thickness plays an important role in determining the durability of coating systems, where variations exceeding ±25% of the nominal thickness can reduce long-term protection effectiveness [26]. Optimal thickness allows for a balance between low permeability and minimal internal stress in the coating. A study by Sulthana et al. [14] shows that increased thickness due to homogeneous nanoparticle distribution prolongs the corrosion initiation time by reducing electrolyte diffusion. These results are consistent with these observations, where S3 with medium thickness showed the lowest corrosion rate. Conversely, excessively thick layers such as S2 are prone to microcracks due to thermal stress and shrinkage during curing, as explained in Hedayatzadeh et al. [24], who reported a decrease in adhesion in coatings with excessive thickness. The positive correlation between moderate thickness and corrosion resistance in the S3 sample emphasizes the importance of controlling the morphology and dispersion of nano-SiO_2 in maintaining coating durability.

Morphology and Elemental Analysis

The EDX analysis after 21 days of immersion in 3.5% NaCl solution revealed signifi-

cant differences in elemental composition between the uncoated steel and the hybrid-coated systems, as summarized in Table 4. The control sample S1 exhibited the highest Fe content (52.31 wt%) and a high O content (38.57 wt%), indicating the formation of corrosion products such as Fe_2O_3 and FeOOH due to direct exposure to chloride ions. This is consistent with the SEM image in Figure 5(a), which shows a rough surface morphology with visible corrosion scales and localized pitting. The highest Cl content (2.70 wt%) further confirms aggressive ion penetration without any diffusion barrier. In contrast, all coated samples showed a substantial reduction in detectable surface Fe, demonstrating the protective function of the coating layer. Sample S3 (100 nm) presented the highest Si content (12.56 wt%), the lowest Fe content (5.21 wt%), and the lowest Cl content (1.13 wt%), confirming the most homogeneous nano-SiO_2 dispersion and the formation of an effective tortuous diffusion pathway that significantly restricts chloride ion penetration. As shown in Figure 5(c), the SEM micrograph displays a compact and dense morphology with minimal microstructural defects. Sample S2 (20 nm) showed lower Si content due to nanoparticle agglomeration leading to microvoid formation. This is reflected in Figure 5(b) as localized surface inhomogeneities and small voids within the coating matrix. In contrast, Sample S4 (500 nm) exhibited relatively higher Fe content as a result of micro-

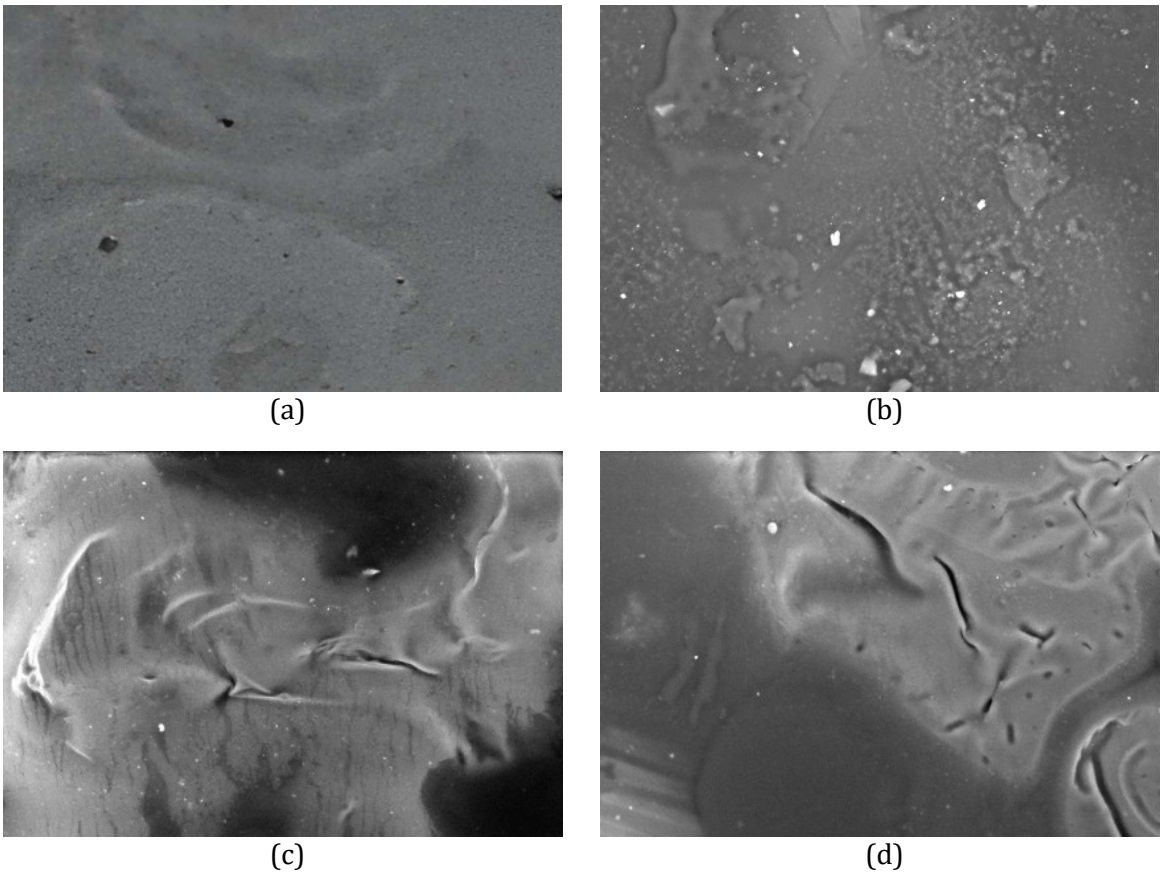

(a) (b) (c) (d)

Figure 5. Comparison of SEM Results of Uncoated Steel and Coated Steel with Different SiO_2 Particle Sizes

Table 4. EDX Elemental Composition of Uncoated of Uncoated Steel and Coated Steel with Different SiO_2 Particle Sizes

Samples	C (wt%)	O (wt%)	Si (wt%)	Fe (wt%)	Cl (wt%)
S1	6.42	38.57	0	52.31	2.70
S2	48.32	32.15	6.84	10.97	1.72
S3	52.47	28.63	12.56	5.21	1.13
S4	46.18	30.74	8.92	12.84	1.32

cracking and particle sedimentation. This is evident in Figure 5(d), where microcracks and surface irregularities indicate partial substrate exposure. Overall, the EDX results strongly support the electrochemical and morphological findings, demonstrating that the 100 nm particle size produces the most stable barrier structure and promotes passive film stabilization, whereas the uncoated steel undergoes a dominant active dissolution mechanism.

Differences in nano-SiO_2 size affect the morphology of the layer and the distribution of elements detected through SEM–EDX because particle size determines dispersion stability and the quality of interaction between the inorganic phase and the polymer matrix. González-Reyna et al. [10] emphasized that the quality of hybrid coatings depends heavily on the size and distribution of silica particles; non-homogeneous dispersion reduces the continuity of the barrier structure. Additionally, smaller particles were found to exhibit lower zeta potential stability than larger particles, increasing their tendency to agglomerate and resulting in microstructural irregularities. SEM images showing inhomogeneity or microdefects under unstable size conditions correlate with this phenomenon, as confirmed by EDX results indicating electrolyte penetration close to the substrate through the continued detection of Fe and Cl. However, González-Reyna et al. [10] also demonstrated that, despite their high surface area, which has the potential to increase adhesion and impedance, small particles' effectiveness in protection is determined by the balance between surface area and distribution homogeneity in the matrix. When particle size is within a more balanced range, dispersion becomes more stable and the coating structure becomes more compact and continuous, resulting in longer and more inhibited ion diffusion pathways. This explains the correlation between denser and more homogeneous SEM morphology and EDX results showing the lowest Fe and Cl content, allowing 100 nm to be identified as the optimum condition because it produces the most effective barrier structure in terms of microstructure and composition.

Corrosion Failure Mechanism

The combined results of electrochemical testing, FTIR, morphology, and thickness measurements indicate that the four specimens (S1–S4) experienced different corrosion failure mechanisms depending on the coating structure and nano-SiO_2 particle size.

Active Dissolution – S1 (Bare Steel)

The active dissolution mechanism in specimen S1 occurred due to direct exposure of steel to a 3.5% NaCl environment without coating protection. The results of research by Buruiană et al. [23] also show that carbon steel immersed in a 3.5% NaCl solution undergoes active dissolution immediately after initial contact, marked by a decrease in corrosion potential and the formation of pits due to chloride ion attack penetrating the natural oxide layer on the surface. Highly reactive chloride ions penetrate the natural oxide layer of steel and form galvanic cells on the surface. This mechanism is strongly supported by SEM–EDX observations, where S1 exhibits the highest Fe content (52.31 wt%), high O content (38.57 wt%), and the highest Cl content (2.70 wt%), indicating the formation of corrosion products such as Fe_2O_3 and FeOOH along with aggressive chloride accumulation near the surface. The SEM morphology further reveals a rough and heterogeneous surface with visible corrosion scales and localized pitting, confirming the absence of any diffusion barrier that could inhibit electrolyte penetration. Tafel test results show the highest i_{corr} and most negative E_{corr} values, indicating no charge transfer resistance and a high corrosion rate. The surface morphology shows large and uniform pits, indicating uniform corrosion. The study by Malla et al. [25] explains that carbon steel undergoes localized corrosion that starts from the initiation point of pits due to the active dissolution of Fe^{2+} ions. This phenomenon is consistent with condition S1, which shows micron-sized pits in areas with high residual stress. Electrochemically, the reaction occurs in the active domain without a significant passive zone on the Tafel curve, and the high Fe

signal detected by EDX confirms continuous metal dissolution rather than passive film stabilization. The rate of corrosion product formation is higher than the steel's ability to form a protective film. As a result, surface damage progressively increases from general corrosion to pitting corrosion. The failure of S1 is dominated by the dissolution of active metals without effective diffusion barriers.

Porous Barrier Breakdown – S2 (20 nm SiO_2)

The porous barrier breakdown mechanism in the S2 specimen was caused by the non-homogeneous layer structure resulting from the use of very small (20 nm) nano-SiO_2 particles. During the mixing process, particles that are too fine tend to agglomerate. This aggregation forms microchannels or microvoids in the castor oil–epoxy matrix, which increases permeability to water and chloride ions. SEM observations after immersion clearly show localized surface inhomogeneities and small voids within the coating matrix, confirming the presence of agglomeration-induced defects. EDX analysis further reveals that the Si content is lower than in S3, while Fe and Cl are still detectably present, indicating that electrolyte penetration reached regions close to the substrate through these microstructural discontinuities. The potentiodynamic polarization test results showed a decrease in i_{corr} compared to uncoated steel, but not as significant as in S3. This indicates that the coating still provides resistance, but it is partial and easily penetrated. FTIR analysis indicated an increase in the intensity of the –OH peak after the corrosion test, indicating water absorption into the polymer matrix. The correlation between increased –OH intensity and detectable Cl in EDX supports the capillary diffusion mechanism through microvoid pathways formed by nanoparticle agglomeration. These findings support the view that particle dispersion inhomogeneity can cause faster barrier breakdown due to the formation of ionic conductive pathways [27], [28]. After immersion in NaCl for 7 days, microcracks began to develop around the pore zone due to internal stress. This process accelerated the penetration of the NaCl solution through capillary mechanisms. Corrosion then occurs under the film and causes local delamination. This failure mechanism is classified as barrier failure type, where the physical barrier function of the film decreases due to uneven particle distribution [29]. Overall, porous barrier breakdown in S2 confirms the importance of controlling nano-SiO_2 dispersion to prevent chloride ion migration pathways within the coating system.

Passive Film Stabilization – S3 (100 nm SiO_2)

Specimen S3 underwent passive film stabilization, a condition in which the coating successfully resisted the penetration of aggressive ions and supported the formation of a stable passive layer at the metal–coating interface. The size of the nano-SiO_2 particles, which is 100 nm, was found to produce the most homogeneous dispersion in the castor oil–epoxy matrix, creating a tortuous path for water molecules and chloride ions [30]. The potentiodynamic polarization test results showed the most positive E_{corr} value (−0.371 V) and the lowest i_{corr} ($1.330\times 10^{-8} A/cm^2$), indicating the highest charge transfer resistance (Rct) among all specimens. The Tafel pattern showed a flat anodic curve, indicating a very low metal dissolution rate due to the formation of a passive layer. This electrochemical behavior is strongly corroborated by SEM–EDX results, where S3 exhibits the highest Si content (12.56 wt%), the lowest Fe content (5.21 wt%), and the lowest Cl content (1.13 wt%), confirming minimal substrate exposure and highly restricted chloride penetration. The SEM micrograph reveals a compact, dense, and uniform morphology with negligible microvoids or microcracks, demonstrating the formation of a continuous barrier layer**.** FTIR showed stable Si–O–Si and –OH peaks without significant shifts, indicating that the chemical integrity of the coating was maintained. A study by Hussain et al. [13] reported that the homogeneous distribution of SiO_2 in the epoxy matrix can increase impedance to $10^{21}\ \Omega\cdot cm^2$ through the formation of a crosslinked barrier network that blocks corrosive ions. The dominance of Si in the EDX spectrum further indicates that the silica-rich outer

layer remained intact after immersion, functioning as the primary diffusion barrier. The morphology of S3 shows localized shallow pits, indicating that the corrosion layer covers most of the surface. Chloride ions attempting to penetrate the layer are blocked by the dense and hydrophilic silica network structure. This mechanism results in a balance between physical and chemical protection, where the passive layer is reinforced by interactions between the hydroxyl groups of castor oil and the silanol groups of SiO_2 [31]. Therefore, passive film stabilization in S3 is an ideal condition where ion diffusion is minimized.

Coating Cracking dan Localized Pitting – S4 (500 nm SiO_2)

Specimen S4 experienced coating cracking and localized pitting failure mechanisms due to a combination of large particle size and high coating thickness. SiO_2 particles measuring 500 nm tended to sediment during the mixing process, causing an inhomogeneous distribution within the coating [32]. The coating thickness of 500 μm created a stress gradient during the drying process, which triggered microcracks at the coating interface. SEM observations clearly reveal microcracks and surface irregularities, indicating partial substrate exposure as a consequence of internal stress and particle sedimentation. EDX results support this finding, showing relatively higher Fe content compared to S3 along with detectable Cl accumulation, confirming that electrolyte penetration occurred through crack pathways. The results of the potentiodynamic polarization test showed an increase in i_{corr} compared to S3, indicating a decrease in barrier effectiveness due to the formation of conductive paths through the cracks. Macroscopic observations reveal fine cracks around the pit area that enlarge after 7 days of NaCl exposure. These cracks accelerate water and ion penetration, triggering localized corrosion under the coating. The pitting mechanism starts from exposed surface defects and develops into microscopic pits around the crack boundaries [33]. The heterogeneous Si distribution detected by EDX further indicates that large particles were not uniformly embedded within the matrix, reducing the continuity of the silica-rich barrier layer. FTIR showed an increase in –OH intensity after corrosion, indicating chemical degradation due to water absorption. ISO 12944-5 confirms that thickness variations exceeding 25% of the nominal value can reduce coating durability and increase the risk of delamination [26]. These results are consistent with the failure pattern of S4, where a thick but inflexible coating caused local loss of adhesion. Additionally, large particle size reduced the ability of SiO_2 to close micro-pores, resulting in shorter ion diffusion paths. This process produces deep local pits with a characteristic corrosion spot pattern beneath the coating. Coating cracking and localized pitting in S4 illustrate mechanical failure due to the interaction between excessive thickness, large particle distribution, and internal coating stress.

CONCLUSIONS

This study systematically evaluated the corrosion resistance performance and failure mechanisms of a hybrid coating system based on castor oil and nano-SiO_2 with different particle size variations applied to ASTM A36 steel. The main findings are summarized as follows:

a. Test results indicate that the coating variant with 100 nm nano-SiO_2 (S3) provides the best anti-corrosion performance, characterized by the lowest i_{corr} value of 1.330×10^{-8}A/cm^2 and the most positive E_{corr} shift, resulting in a corrosion rate reduction of one order of magnitude compared to uncoated steel or other variants.
b. The superior performance of S3 is attributed to the homogeneous dispersion of 100 nm nano-SiO_2, which produces a compact and continuous coating structure and forms an effective tortuous diffusion pathway. SEM–EDX analysis indicates minimal substrate exposure after immersion, while FTIR spectra show stable Si–O–Si and –OH functional

groups without significant shifts, confirming that the chemical integrity of the hybrid network is maintained. The combination of microstructural continuity and chemical stability promotes passive film stabilization at the metal–coating interface.

c. These findings confirm that controlling the size and dispersion of nano-SiO_2 is a key factor in improving the effectiveness of hybrid castor oil–epoxy coatings. The 100 nm size has been proven to best balance coating thickness, compactness, and chemical stability, thereby providing long-term protection against corrosion. These results form an important technical basis for the development of high-performance bio-nano coatings that prioritize sustainability, durability, and compatibility for structural applications in aggressive environments.

ACKNOWLEDGEMENTS

DECLARATION OF CONFLICTING INTERESTS

The authors declare that they have no potential conflicts of interest regarding the research, authorship, and/or publication of this article.

FUNDING

REFERENCES

[1] P. Liu, Q. H. Zhang, Y. Watanabe, et al., "A critical review of the recent advances in inclusion-triggered localized corrosion in steel," Dec. 01, 2022, *Nature Publishing Group*. doi: 10.1038/s41529-022-00294-6.

[2] S. Huang, J. Liu, L. Wen, *et al.*, "Electrochemical properties and corrosion induced mechanical degradation of biomedical Zn–Cu–Li alloy in simulated body fluid," *Mater. Des.*, vol. 244, Aug. 2024, doi: 10.1016/j.matdes.2024.113161.

[3] Direktorat Teknik dan Lingkungan Migas, "ATLAS Keselamatan Migas Vol.5," 2024.

[4] O. O. Joseph, S. Banjo, S. A. Afolalu, et al., "Global and Economic Effects of Corrosion - An Overview," in *AIP Conference Proceedings*, American Institute of Physics Inc., Aug. 2022. doi: 10.1063/5.0092286.

[5] M. K. El Kouifat, H. Zniker, and M. El Hasnaoui, "Corrosion failure analysis of steel tubes operating in mining installations: Metallurgical, chemical and mechanical investigations," *International Review of Applied Sciences and Engineering*, vol. 16, no. 2, pp. 225–232, Jun. 2025, doi: 10.1556/1848.2024.00903.

[6] F. Al-Abkal and A. Husain, "Failure analysis of corroded underground pipeline," in *Materials Research Proceedings*, Association of American Publishers, 2025, pp. 539–548. doi: 10.21741/9781644903414-59.

[7] Q. Hu, S. Yang, W. Zhang, et al., "Corrosion failure analysis of engineering structural steels in tropical marine atmospheres: A comparative study of ordinary and new weathering steels," *Eng. Fail. Anal.*, vol. 156, p. 107830, 2024, doi: https://doi.org/10.1016/j.engfailanal.2023.107830.

[8] Y. Yang, C. Chen, Y. Zhuang, et al., "Reviewing the progress of corrosion fatigue research on marine structures," 2024, *Frontiers Media SA*. doi: 10.3389/fmats.2024.1399292.

[9] M. A. Alam, U. A. Samad, A. Anis, et al., "Effects of SiO2 and ZnO nanoparticles on epoxy coatings and its performance investigation using thermal and nanoindentation technique," *Polymers (Basel).*, vol. 13, no. 9, May 2021, doi: 10.3390/polym13091490.

[10] M. A. González-Reyna, M. A. Espinosa-Medina, R. Esparza, et al., "Anticorrosive Effect of the Size of Silica Nanoparticles on PMMA-Based Hybrid Coatings," *J. Mater. Eng. Perform.*, vol. 30, no. 2, pp. 1054-1065, Feb. 2021, doi: 10.1007/s11665-020-05437-x.

[11] Y. Wang, M. Li, and Y. Xiong, "Enhancement of barrier and corrosion protection properties of epoxy coatings by aminofunctionalized silica nanoparticles in epoxidized eucommia ulmoides gum/epoxy double crosslinked networks," *J. Mater. Sci.*, vol. 60, no. 10, pp. 4625–4644, Mar. 2025, doi: 10.1007/s10853-025-10690-3.

[12] Y. Xu, D. Gao, Q. Dong, *et al.*, "Anticorrosive behavior of epoxy coating modified with hydrophobic nano-silica on phosphatized carbon steel," *Prog. Org. Coat.*, vol. 151, Feb. 2021, doi: 10.1016/j.porgcoat.2020.106051.

[13] Z. Hussain, Z. Lin, H. Pan, et al., "Synergizing empirical and AI methods to examine nano-silica's microscale contribution to epoxy coating corrosion resistance," *Ceram. Int.*, vol. 50, no. 22, pp. 47172–47191, Nov. 2024, doi: 10.1016/j.ceramint.2024.09.067.

[14] Y. R. Sulthana, D. K. Chelike, and S. A. Gurusamy Thangavelu, "Biorenewable vegetable oil based nonisocyanate polyurethanes and nanocomposites; formulation, characterisation, biodegradation, anticorrosion and antifouling coatings," *New Journal of Chemistry*, vol. 48, no. 12, pp. 5173–5185, Feb. 2024, doi: 10.1039/d3nj05862j.

[15] Ż. Ciastowicz, R. Pamuła, Ł. Bobak, et al., "Characterization of Vegetable Oils for Direct Use in Polyurethane-Based Adhesives: Physicochemical and Compatibility Assessment," *Materials*, vol. 18, no. 5, Mar. 2025, doi: 10.3390/ma18050918.

[16] X. Wei, J. Ge, F. Gao, *et al.*, "Bio-based self-healing coating material derived from renewable castor oil and multifunctional alamine," *Eur. Polym. J.*, vol. 160, p. 110804, 2021, doi: https://doi.org/10.1016/j.eurpolymj.2021.110804.

[17] Z. Li and Z. Li, "EIS and potentiodynamic polarization studies of arc-sprayed aluminum coating on Q235 steel surface," *Int. J. Electrochem. Sci.*, vol. 18, no. 3, 2023, doi: 10.1016/j.ijoes.2023.100058.

[18] P. Manik, D. Chrismianto, and P. F. Prayoga, "The Influence of SMAW Welding Current Variation on Tensile Strength, Corrosion Rate, and Microstructure of ST 42 Steel for Inner Bottom Plate Material in Ships," 2023.

[19] J. Villegas-Tovar, C. Gaona-Tiburcio, M. Lara-Banda *et al.*, "Electrochemical Corrosion Behavior of Passivated Precipitation Hardening Stainless Steels for Aerospace Applications," *Metals (Basel).*, vol. 13, no. 5, May 2023, doi: 10.3390/met13050835.

[20] Y. Gong, X. Chen, and W. Wu, "Application of fourier transform infrared (FTIR) spectroscopy in sample preparation: Material characterization and mechanism investigation," *Advances in Sample Preparation*, vol. 11, Aug. 2024, doi: 10.1016/j.sampre.2024.100122.

[21] B. Li, L. Fan, Y. Wen, *et al.*, "Study of Morphology and Corrosion Behavior of Aluminum Coatings on Steel Substrates under Simulated Acid Rain Conditions," *Metals (Basel).*, vol. 13, no. 3, Mar. 2023, doi: 10.3390/met13030613.

[22] P. Lin and X. Chen, "Experimental and Modeling Analysis of the Tensile Properties of Heavy-Duty Coatings for Steel Structures," *Coatings*, vol. 14, no. 10, Oct. 2024, doi: 10.3390/coatings14101289.

[23] D. L. Buruiană, A. C. Mureșan, N. Bogatu, et al., "Corrosion Tendency of S235 Steel in 3.5% NaCl Solution and Drinking Water During Six Months of Exposure," *Materials*, vol. 17, no. 23, Dec. 2024, doi: 10.3390/ma17235979.

[24] M. H. Hedayatzadeh, M. Sepehrian, and M. Anbia, "Investigation of sol-gel derived organic inorganic hybrid coatings based on commercial epoxy resin for improved corrosion resistance of 304 stainless steel," *Sci. Rep.*, vol. 15, no. 1, Dec. 2025, doi: 10.1038/s41598-025-90861-z.

[25] A. D. Malla, J. H. Sullivan, D. J. Penney, *et al.*, "Mechanistic investigation on the influence of coating weights on the corrosion behaviour of hot-dip-galvanised Zn-

Mg-Al coatings," *Npj Mater. Degrad.*, vol. 8, no. 1, Dec. 2024, doi: 10.1038/s41529-024-00494-2.

[26] ISO, "Paints and varnishes - Corrosion protection of steel structures by protective paint systems Part 5: Protective paint systems," 2018.

[27] M. C. Uvida, A. de A. Almeida, S. H. Pulcinelli, et al., "Structural Properties of Epoxy–Silica Barrier Coatings for Corrosion Protection of Reinforcing Steel," *Polymers (Basel).*, vol. 14, no. 17, Sep. 2022, doi: 10.3390/polym14173474.

[28] R. R. Abakah, F. Huang, Q. Hu, et al., "Comparative study of corrosion properties of different graphene nanoplate/epoxy composite coatings for enhanced surface barrier protection," *Coatings*, vol. 11, no. 3, pp. 1–18, Mar. 2021, doi: 10.3390/coatings11030285.

[29] M. Petrunin, T. Yurasova, A. Rybkina, et al., "Specifics and Methods of Inhibiting the Underfilm Corrosion of Carbon Steel," *Polymers (Basel).*, vol. 16, no. 6, Mar. 2024, doi: 10.3390/polym16060780.

[30] R. Gautam, A. Hazra, P. Faujdar, *et al.*, "Effect of Size-Controlled Nanofluid on Mechanical Properties, Microstructure, and Rheological Behavior of Cement Slurry for Oil Well Cementing," *ACS Omega*, vol. 9, no. 48, pp. 47739–47755, Dec. 2024, doi: 10.1021/acsomega.4c07871.

[31] E. Laurent and M. Maric, "Organic–Inorganic Hybrid Materials from Vegetable Oils," Dec. 01, 2024, *John Wiley and Sons Inc*. doi: 10.1002/marc.202400408.

[32] H. Chen, X. Jia, M. Fairweather, et al., "Characterising the sedimentation of bidisperse colloidal silica using analytical centrifugation," *Advanced Powder Technology*, vol. 34, no. 2, Feb. 2023, doi: 10.1016/j.apt.2023.103950.

[33] O. Loukil, L. Adelaide, V. Bouteiller, et al., "Investigation of Corrosion Product Distribution and Induced Cracking Patterns in Reinforced Concrete Using Accelerated Corrosion Testing," *Applied Sciences (Switzerland)*, vol. 14, no. 23, Dec. 2024, doi: 10.3390/app142311453.